nature electronics

Article

https://doi.org/10.1038/s41928-025-01481-4

Metaphotonic photodetectors for direct Stokes quantification

Received: 25 December 2024

Accepted: 16 September 2025

Published online: 20 October 2025

Check for updates

Xingsi Liu[1], Yinzhu Chen[1,2], Xianghong Kong[1], Weixin Liu[1], Zhenhua Ni[2], Junpeng Lu[2], Qi Jie Wang[3], Chengkuo Lee[1], Jingxuan Wei[4] ✉ & Cheng-Wei Qiu[1] ✉

Metaphotonics uses nanoengineered materials to manipulate the electromagnetic fields and is of use in multidimensional optoelectronic applications such as Stokes detection. Machine learning algorithms are often used in the device design and post-signal processing of these systems. During post-signal processing, such algorithms can be used to reconstruct the physical quantities from multiparameter optical responses, typically via inversion of the system's response function. However, when response channels are coupled or signal amplitudes vary greatly, post-detection decoding becomes difficult due to potential information loss. Here we report a metaphotonic photodetector capable of direct Stokes quantification. We use channel-level decoupling to design independent photovoltage channels for each Stokes parameter with minimal crosstalk. The device responsivity matrix achieves a near-unity condition number, reducing reliance on complex algorithmic post-processing. Our approach illustrates how device-level optimization can enhance detection capabilities in parallel with algorithmic techniques.

Machine learning is used in optoelectronic technologies for signal decoding, inverse design and performance enhancement. It can accelerate electromagnetic solvers[1–5], assist in the design of metamaterials[6–8] and provide efficient signal post-processing[9–12]. It can, thus, help improve optoelectronic systems such as photodetectors[13,14], optical communication devices[15,16] and imaging systems[17–19].

In multiparameter optical measurements, a typical reconstruction strategy is to invert the response matrix to estimate the contributions of each physical quantity from the measured signal. Common methods include matrix inversion[20–23], arithmetic estimation[24–26] and learning-based approaches[27–29]. However, the effectiveness of post-detection inversion remains strongly dependent on whether the encoded signals are adequately separated at the measurement stage[30–32].

In particular, post-detection decoding becomes difficult when response channels are coupled or when some components exhibit much lower amplitudes. In such cases, weaker signals may be irreversibly buried during acquisition, making them unrecoverable, even with algorithmic inversion that closely approximates the ideal solution. This reflects a fundamental constraint: from an information-theoretic perspective, recoverable content is bounded by what is captured, so no algorithm can retrieve information that was never recorded.

Here we report a metaphotonic photodetector that can provide distinct, decoupled responses for each Stokes parameter. The Stokes vector $\mathbf{S} = (S_0, S_1, S_2, S_3)^{\mathrm{T}}$ offers clear physical importance in polarization detection[23,33,34], and its linear and complete representational form makes it an ideal platform for examining signal decoupling. We design a direct-full-Stokes photodetector using four sub-detectors to cover the complete four-element Stokes vector, and each sub-detector is immune to crosstalk from the other components. The sub-detectors are based on metal nanostructures with meandering geometrical arrangements on top of a graphene layer, which fill up a single pixel and form a spatially compact, co-located detector array (Fig. 1a–d).

[1]Department of Electrical and Computer Engineering, National University of Singapore, Singapore, Singapore. [2]Key Laboratory of Quantum Materials and Devices of Ministry of Education, School of Physics, Southeast University, Nanjing, China. [3]School of Electrical and Electronic Engineering, Nanyang Technological University, Singapore, Singapore. [4]School of Optoelectronic Science and Engineering, University of Electronic Science and Technology of China, Chengdu, China. ✉e-mail: jxwei@uestc.edu.cn; chengwei.qiu@nus.edu.sg

https://doi.org/10.1038/s41928-025-01481-4

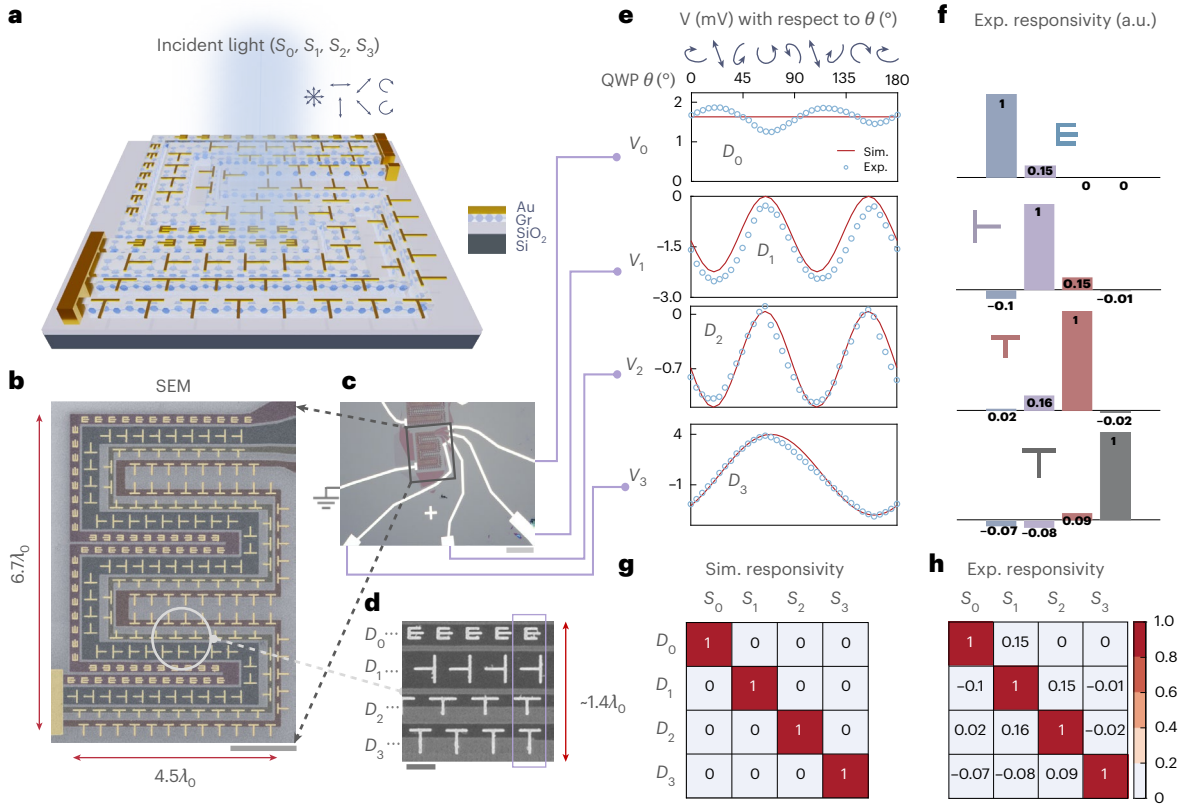

Fig. 1 | Direct Stokes photodetection using nanostructures atop graphene. **a**, Schematic of the single-pixel direct-full-Stokes photodetector composed of four groups of engineered nano-optoelectronic structures fabricated on graphene. Under normally incident mid-infrared illumination at a wavelength of 4 μm (λ_0), with arbitrary polarization states including polarized and unpolarized light (indicated by arrows), four output signals are generated without external bias. Each signal corresponds to one of the Stokes parameters (S_0–S_3) of the incident light. **b**, SEM image of the device. Scale bar, 5 μm. **c**, Optical image of the device showing the electrode layout. Scale bar, 20 μm. **d**, Zoomed-in SEM image of the boxed region in **b**, showing the super-unit structure composed of four sub-devices D_0–D_3. Scale bar, 1 μm. **e**, Simulated (Sim.) and experimentally measured (Exp.) photovoltage responses V_0–V_3 when rotating the quarter-wave plate (QWP) with rotation angle θ. The sub-devices D_0–D_3 exhibit uniform S_0 response and near-ideal photovoltage responses V_1–V_3 for S_1–S_3, respectively. **f**, Extracted and normalized response vectors of each sub-device, presented in arbitrary units (a.u.). **g**,**h**, Simulated (**g**) and experimentally measured (**h**) responsivity matrices for sub-devices D_0–D_3, normalized for visualization. Each row corresponds to the Stokes responsivity of one sub-device. The device exhibits an approximately diagonal 4 × 4 responsivity matrix, showing near-direct mapping between the incident Stokes vector and the photovoltage output vector.

The vectorial photoresponse arises from near-field-to-photocurrent transitions, which are enabled by symmetry engineering and mode profile control. The system, thus, one-to-one maps electrical outputs and Stokes parameters, with experimentally verified bipolar S_1–S_3 and uniform S_0 signals. The resulting response matrix R is near-diagonal and well conditioned, supporting direct Stokes read-out with minimal noise amplification and isotropic information distribution[30,35]. Our direct-full-Stokes detector has a composite responsivity of 14,579.2 $V^4\,W^{-4}$, defined as the determinant of R, whereas the incident power for each R_{ij} is calculated based on the total area of the device (Fig. 1b,c). At zero source–drain bias and zero gate voltage, the direct Stokes detector demonstrates the maximum measured responsivity of 116.7 $V\,W^{-1}$ with a signal-to-noise ratio on the order of 500 under incident power of hundreds of microwatts. It can be used as a passive, room-temperature and power-efficient platform for real-time, in situ polarization analysis in integrated mid-infrared photonic systems.

Responsivity zeroing design

Figure 1a provides an illustration of our single-pixel direct-full-Stokes photodetector, with an optical image and scanning electron microscopy (SEM) image of one device shown in Fig. 1b. Four signals are collected (Fig. 1c,e), each corresponding to the photovoltage detection for one Stokes parameter. Every sub-detector $D_i, i \in (0, 1, 2, 3)$consists of one group of specifically designed metal nanostructures with a meandering arrangement atop graphene, and represented by one row $\mathbf{R}_i$ in the system responsivity matrix R. The system can be expressed as follows:

$$\begin{bmatrix} V_0 \\ V_1 \\ V_2 \\ V_3 \end{bmatrix} = \begin{bmatrix} R_{00} & R_{01} & R_{02} & R_{03} \\ R_{10} & R_{11} & R_{12} & R_{13} \\ R_{20} & R_{21} & R_{22} & R_{23} \\ R_{30} & R_{31} & R_{32} & R_{33} \end{bmatrix} \begin{bmatrix} S_0 \\ S_1 \\ S_2 \\ S_3 \end{bmatrix}, \quad (1)$$

where V_i represents the photovoltage measured from ith port and S_i is the ith Stokes parameter. The use of using a 4 × 4 responsivity matrix representation to our direct Stokes detectors is supported by prior research in which the graphene photocurrent demonstrated a linear relationship with incident power over a substantial range[36,37].

The design principle of our system, as suggested by the name 'responsivity-matrix-diagonalizing' design, requires zeroing the 12 off-diagonal elements in R. Namely, each nanostructure, one row of R, is to distribute three zeros out of its four-element responsivity vector, leading to the direct detection of Stokes parameter with single non-zero responsivity. This implies that the collected photoresponse for one Stokes parameter remains constant if other Stokes parameters vary.

https://doi.org/10.1038/s41928-025-01481-4

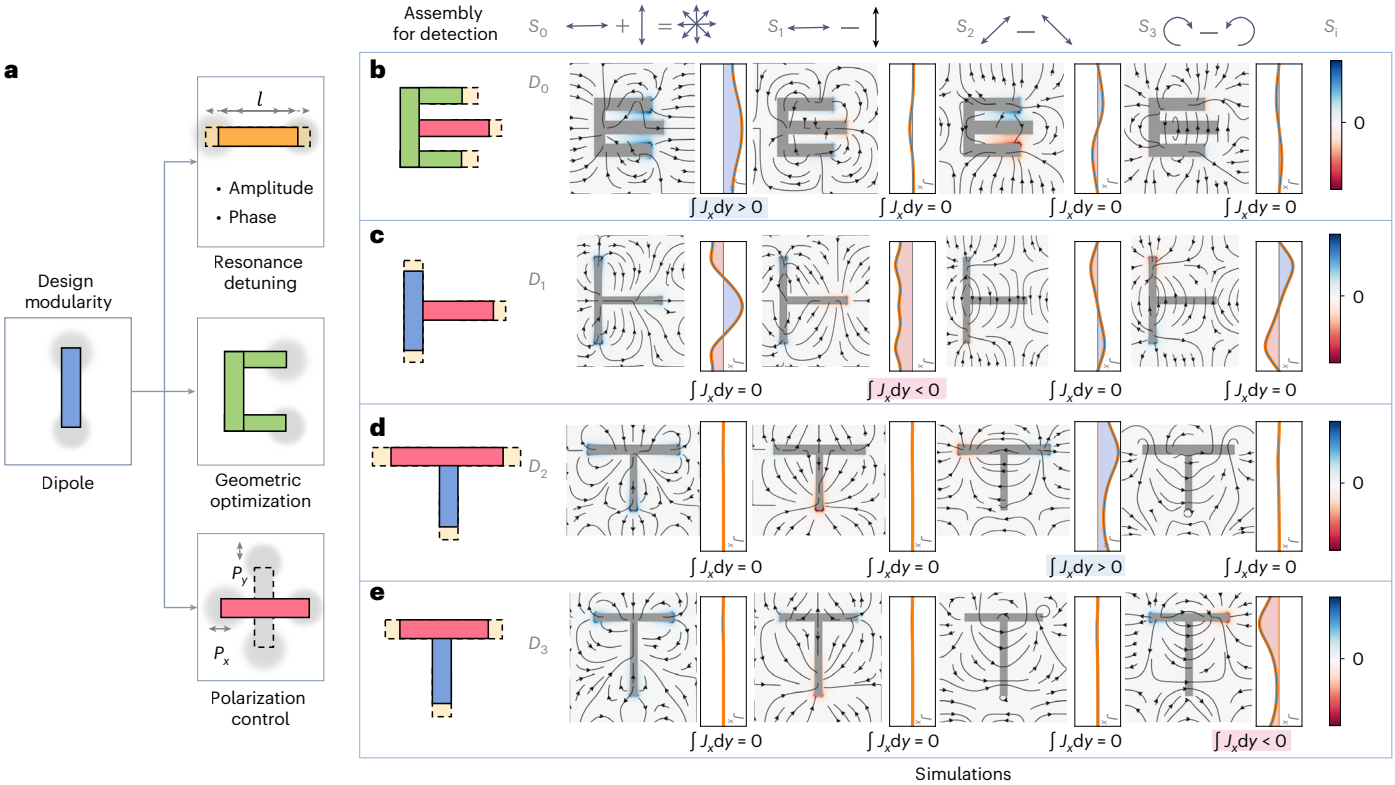

Fig. 2 | Design flow of plasmonic structures for diagonalizing *R*. a, Basic dipole plasmonic unit: a rectangular bar with tunable length and orientation. By adjusting these parameters and combining units, the desired responsivity responses can be achieved. **b**–**e**, Optimized plasmonic structures for sub-devices D_0–D_3 designed for the direct detection of the four Stokes parameters (S_0–S_3) are shown (left). The corresponding simulated near-field distributions and *x*-direction photocurrent flow (J_x) along a *y*-oriented cutline are shown (right). For each design, the net J_x is non-zero only for the target Stokes parameter, whereas the photocurrent responses to the other parameters are zero due to symmetry or cancellation. This leads to a diagonal **R** with all off-diagonal elements suppressed, enabling direct Stokes photodetection.

To guide the design, we first analyse the mechanisms responsible for photoresponse generation. The encoding procedure from arbitrary Stokes vector **S** into a four-element photoresponse vector **V** comprises two steps: (1) optical transformation in which the incident light interacts with the nanostructure, generating an optical near-field, and (2) subsequent optical-to-electrical conversion taking advantage of materials such as graphene[38–41]. In the first step, the near-field of the metallic nanostructures exhibits distinct profiles for different Stokes vector **S** when subjected to a normally illuminated incident wave. This diversity in profiles raises from the ability of incident **S** to excite multiple eigenmodes with varying weights, leading to interference effects that manifest as intensity profiles. In the second step, the localized optical near-field excites hot electrons that flow leveraging patterned graphene with the metal nanostructure atop and generate a photocurrent. This step provides vectorial degrees of freedom in controlling the spatial distribution and directionality of the photocurrent. This optical-to-electrical conversion and the photoresponse simulation have been well established in prior research[42–44], and is used in our optimization in subsequent sections.

In our study, we achieve the desired distribution of electric field intensity through the design of plasmonic nanostructures with precisely tailored geometries (Fig. 2a). The foundation of our design lies in a bar-shaped structure, serving as the primary modular unit that supports the fundamental dipole mode. Building on this foundation, we use three further adjustments to tailor the structure: resonance detuning achieved by adjusting the structure's length, thereby modifying the amplitude and phase of the excited modes; geometric optimization by appending small modules at the ends to shift the position of the dipole mode's high-intensity focus; and polarization control by rotating the structure to allow the dipole mode to respond to incident light of varying polarization directions.

By integrating these adjustments, we can design the electric field intensity distribution to achieve zero responsivities for various Stokes parameters. This approach includes two steps: optical transformation and optical-to-electrical conversion. Initially, symmetry in the optical intensity near-field distribution can stem from Stokes parameters (polarization), the direction of current measurement and structural symmetry, along with the orthogonality of excited modes. Achieving this symmetry ensures a uniform photoresponse across different polarizations, thereby nullifying the Stokes responsivities. Second, even if the intensity patterns lack symmetry across two polarizations, the collected photoresponse as the integration of currents (including all in-plane currents) can still result in equal or oppositely equal values, fulfilling the condition for zero Stokes responsivities. Details are provided in Supplementary Notes 1–3 and Supplementary Fig. 9.

Figure 2b–e shows four distinct structures resulting from the assembly of bar-shaped structures, corresponding to four sub-device units D_0–D_3 that directly detect S_0–S_3, respectively. Despite both sub-device units D_2 and D_3 being T shaped, their size differences allow them to directly respond to S_2 and S_3, respectively. The plotted equivalent optical near-field intensity profile to each S_i in Fig. 2b–e is derived by adding or subtracting intensity distributions under the respective polarizations (Supplementary Fig. 9). The simulated directions of the equivalent electric current flow are also illustrated as arrows in the plots. Considering that experiments measure current in the *x* direction, the currents at the right boundary (identical to the left due to periodic boundary conditions) predict the experimental outcomes, which are plotted on the right of each simulated mode profile. The integral of those boundary currents indicates that for the 4 × 4 elements in *R*, aside

from the diagonal currents, all off-diagonal currents are either negligible or cancelled out, resulting in a zero net current. Thus, our methodology diagonalizes R, enabling the direct detection of full-Stokes parameters, showcasing a modular assembly approach akin to piecing together building blocks to achieve the desired outcome.

Geometry enabling responsivity zeroing

To complete our nanostructure design with their exact geometric dimensions under an incident wave of $\lambda_0 = 4$ μm, we swept the parameters of the four proposed geometric shapes and calculated their photoresponse vectors. Similar to the previous section, this process involves a two-step simulation for each parameter combination of geometric structure: first, the optical process, from incident light to the optical field profile, and the subsequent optical-to-electrical conversion. The simulated photoresponse allows us to extract the four-element response vectors within the basis of Stokes parameters. Additionally, the width of each plasmonic bar remains at 100 nm, the height at 60 nm and the distance between adjacent structures at 600 nm to avoid involving complicated mutual modes.

For D_1 to D_3 with optimization of the T shape, we tuned the length of its two bars (one vertical and one horizontal). This length variation modulates the pseudo-dipole resonance modes of the bar shape. For D_0, which involves a rotated E shape (or more accurately, 凵 shape, resembling the Chinese character 凹), we kept the bottom bar of 凵 at 475 nm and adjusted the heights of the main and side vertical bars. When the side peak's height is set to zero, the 凵 shape effectively reduces to the inverted T shape. Importantly, during these adjustments, the symmetry is always maintained.

The sixteen R_{ij} responsivity elements under different geometrical setups are displayed in Fig. 3. We consistently observed eight groups of R_{ij} elements that remain as zeros, denoted as symmetry-protected zeros (SPZ), regardless of the variation in shape dimensions. In the case of R_{01}, R_{10}, R_{23} and R_{32}, we observed various R_{ij} values in blue ($R_{ij} > 0$) and red ($R_{ij} < 0$) with different dimension combinations. With finer size adjustment, there must be a line in the plot for which $R_{ij} = 0$ between the red and blue regions, represented by white colour. In light of these results, the nanostructures characterized by the dimensions outlined along those distinct white lines emerge as compelling candidates for the construction of zeroing-responsivity direct-full-Stokes photodetector.

The selection of the most suitable structure is based on specific design goals. To maximize the photoresponse, we selected the candidate with the highest R_{ii} value, marked by stars in the plots. The choice of the optimal structure may also consider additional criteria, such as uniform response magnitude and robustness to geometric variation.

Experiment validation

Our design utilizes optoelectronic nanostructure units together with patterned graphene to effectively direct the flow of current between the units. By adopting various arrangements, we aim to maximize the fill factor, using configurations ranging from conventional straight lines[45] to arbitrary space-filling curves. Specifically, we group four sub-devices into a single super-unit (Fig. 1d, columns) with dimensions of approximately $0.5\lambda_0 \times 1.4\lambda_0$, where λ_0 is the working wavelength as 4 μm. As a demonstration (Fig. 1b–d), these super-units are interconnected in a meandering pattern to fill a space of $6.7\lambda_0 \times 4.5\lambda_0$, equivalent to a 26.8 μm × 18 μm structure at a wavelength of 4 μm (beam spot shown in Supplementary Fig. 10), where further measurements are conducted. Moreover, during the meandering process, the direction of current changes at the turns, necessitating corresponding rotations of the structures to align with their polarization dependencies shown in Supplementary Fig. 11. This layout enables precise control of current flow paths and offers flexibility to meet various device design requirements.

To validate our design, we conducted experiments using the setup illustrated in Supplementary Fig. 8a. A 4-μm laser source generated linearly polarized light, and the polarization state of the light could be modified using a quarter-wave plate. The focused light was directed onto our fabricated device. The polarization and, thus, the Stokes parameter trajectory would change when rotating the wave plate. We quantified the photovoltage response through a systematic rotation of the wave plate by 180°, with an incremental step of $\Delta\vartheta = 5°$. The measured photoresponse is indicated as scattered data points, whereas the corresponding simulated references are highlighted as red curves (Fig. 1e). The D_0 sub-detector would yield consistent responses for all different polarizations, accomplishing isotropic responses for S_0 with an anisotropic structure design, whereas the $D_{1,2}$ sub-detector responses behave as $\sin(4\theta)$ waves. Similarly, for the D_3 detector, the response was expected to follow the $\cos(2\theta)$ trends with respect to the rotation angle. Furthermore, we extracted the responsivity vectors from the measured data and combined them into one 4 × 4 responsivity matrix (Fig. 1f,h), revealing high R_{ii} values and near-zero R_{ij} values. These slight deviations from the simulated diagonal matrix shown in Fig. 1g could be attributed to fabrication errors, inaccuracies in the wave plates and random noise from experiments. Nevertheless, our experimental data closely align with expected Stokes parameters, demonstrating the effectiveness of our direct Stokes photodetectors for full polarization.

We experimentally evaluated the on-chip direct-full-Stokes photodetector, demonstrating high performance across key metrics. The device demonstrated an experimental composite responsivity of 14,579.2 $V^4\,W^{-4}$ with zero bias, defined by the determinant of R, with the incident power for each R_{ij} calculated based on the device's total area (Fig. 1b). Direct detection responsivity across the devices averaged at 12.16 $V\,W^{-1}$, highlighting a sensitive electrical signal output in response to incident light. In particular, the D_0 device, with its meandering arrangement of nanostructures (Supplementary Fig. 12), exhibited a measured responsivity of 116.7 $V\,W^{-1}$ without external bias and gate tuning. This performance exceeds that of commercial mid-infrared photodetectors (Supplementary Table 1). Moreover, the measured signal-to-noise ratio reached around 500 under incident power levels of hundreds of microwatts. In terms of circular polarization detection, the photoresponse discrimination ratio, defined as $g_{ph} = |(J_{LCP} - J_{RCP})/(J_{LCP} + J_{RCP})|$, reached 15.3 for sub-device D_3 (Fig. 1), and even larger for the R_3-specific devices fabricated. For sub-devices D_1 and D_2, the calculated polarization ratios, capturing the ratio of maximum and minimum polarization-dependent photoresponses (at x/y and 45°–45° polarizations), were −1.13 and −1.05, respectively. This ensures the device's capability to accurately distinguish between different polarization states, thereby precisely detecting Stokes parameters. The device's response time is approximately 1 μs, which is crucial for applications requiring real-time measurements. Further performance data are available in Supplementary Note 4 and Supplementary Figs. 13–15.

Full-Stokes imaging demonstration

In conventional polarization imaging systems, photodetectors are typically combined with external polarization filters. By contrast, our on-chip single-pixel photodetector integrates polarization response and electrical signal output functionalities within a compact unit, eliminating the need for external filtering components. Leveraging advanced microelectronics integration technology, our four-port direct-full-Stokes photodetector can serve as a unit pixel to be configured in an array format, enabling the capture of complete polarization images in a single shot. Figure 4a illustrates the imaging system setup, utilizing our single pixel as the photodetector. Through a sweeping method, this setup demonstrates the device's capability to detect various polarizations and produce four simultaneous read-outs forming four Stokes parameter images.

The demonstration experiment comprises an incident light source, a metasurface-based phase plate object, a lens and our designed

https://doi.org/10.1038/s41928-025-01481-4

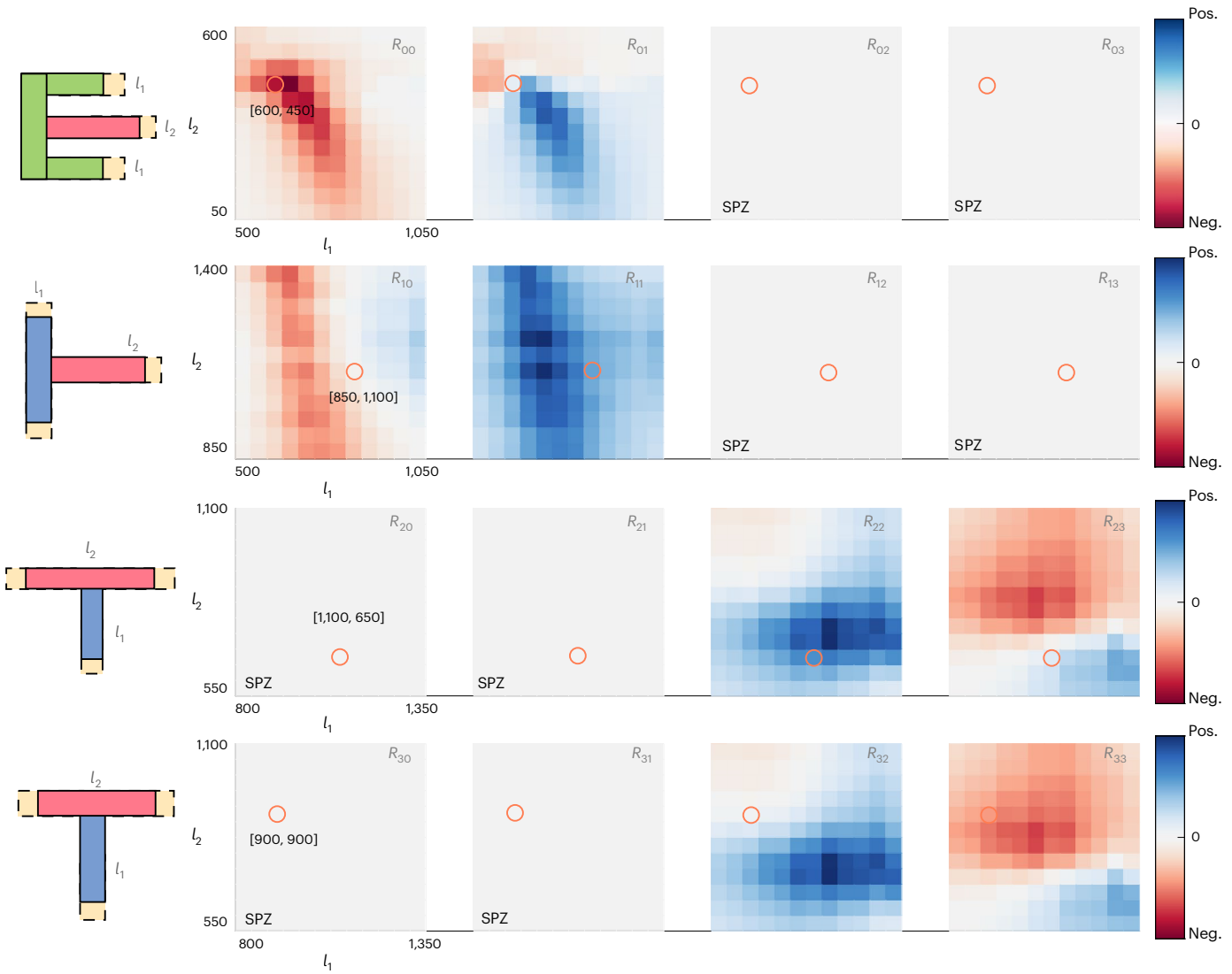

Fig. 3 | Simulated *R* values for sweeping the geometric dimension of the designed plasmonic structures. Simulated values of responsivity matrix *R* are shown as a function of bar lengths l_1 and l_2. R_{ij} values are determined from the simulated photoresponses under varying incident polarizations. Symmetry engineering results in eight SPZ regions in R_{ij}, which appear as strict zeros across all sweeps. In regions where symmetry does not enforce a zero response, both positive and negative R_{ij} values are observed, with zero-responsivity crossings located at boundaries between the differently coloured regions. Optimized structure dimensions are marked by circles. Pos., positive; Neg., negative.

photodetector. The metasurface phase plate is constructed from metallic nanostructures on a CaF_2 substrate, which is transmissive in the mid-infrared range. The phase plate features three groups of structures forming the letters 'nus', with the smallest feature size being 300 μm (Fig. 4b). The imaging system has an object distance of ~50.0 cm and an image distance of ~10.8 cm. The incident light is *x* polarized at 4 μm. Due to experimental limitations, we swept the object and kept the other optical components fixed to realize the single-pixel imaging demonstration. As shown in Fig. 4c, a single scan captures the complete polarization information through images formed by four photovoltage signals measured corresponding to $S_0 - S_3$. The observed aberrations are primarily due to the non-ideal optical path of the system.

To better illustrate the detector's performance with different polarizations, four distinct positions (P_1–P_4) on the phase plate are marked (Fig. 4b). The SEM images of the metallic nanostructures at these positions are shown in Fig. 4d. The design of the metallic meta-atoms follows the work referenced in ref. 46 and is optimized for a 4-μm wavelength. The point P_4 comprises only CaF_2 as the substrate. Consequently, the incident light was transmitted through the metasurface at these positions and carried different polarization states to be detected. Figure 4e presents the photovoltage signals for P_1–P_4, with each row demonstrating the detected polarization response for each position, showcasing the device's capability of effectively distinguishing between distinct polarization states.

Overall, this experiment demonstrates our photodetector's ability to capture full-Stokes parameters and its potential as a single unit in a polarization imaging camera. Compared with commercial polarization detectors, the device features a compact footprint (down to the wavelength scale, determined by the super-period of the four sub-devices (Fig. 1d)) with low channel crosstalk by eliminating the off-diagonal terms in *R*. These characteristics enable high spatial resolution and precision in polarimetric imaging applications.

Conclusions

In multiparameter optical measurements, direct detection theoretically preserves the maximum information content present in the input signal, thereby defining the upper limit of achievable system performance. In practical implementations, near-direct detection

https://doi.org/10.1038/s41928-025-01481-4

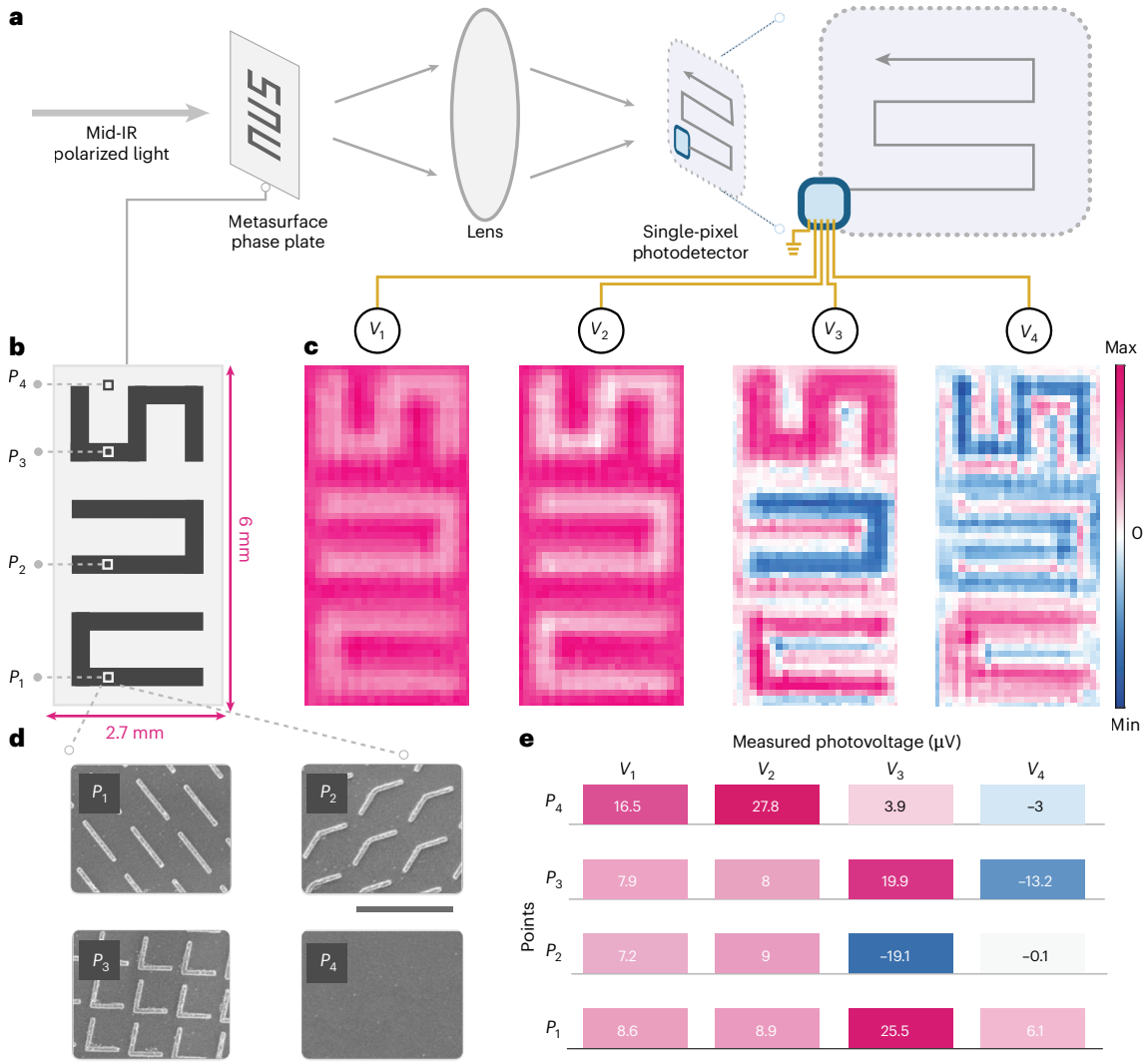

Fig. 4 | Full-Stokes imaging using a single-pixel direct-full-Stokes photodetector. a, Schematic of a full-Stokes imaging system under infrared (IR) illumination using spatial scanning of a single-pixel photodetector. **b**, Metasurface-based phase plate with four marked points P_1–P_4, each exhibiting distinct phase responses. **c**, Measured images obtained from photovoltage responses of the four detection channels. **d**, Zoomed-in SEM images at points P_1–P_4, showing distinct metal meta-atom patterns corresponding to different phase responses. Scale bar, 3 μm. **e**, Measured photovoltages at P_1–P_4, demonstrating that signals from four channels are captured simultaneously in a single acquisition.

architectures with channel-level decoupling can be further combined with post-processing algorithms to enhance detection accuracy and flexibility. Direct detection itself is not a new concept. Traditional intensity measurement methods, along with recent structural designs targeting specific polarization states (such as circular polarization[44,47]), are examples of direct encoding approaches that are sensitive to a particular parameter and remain invariant to certain non-target variables. Our work extends this concept to full-Stokes detection, implementing a compact and channel-isolated architecture that brings direct detection into multidimensional detection.

Our design is based on optimizing R such that $R \approx c\mathbf{I}$, where c is a scalar and I represents identity matrix. This configuration ensures uniform channel response and balanced sensitivity across all Stokes parameters, minimizing numerical instability and reducing crosstalk in practical implementations. It also simplifies system calibration and provides direct parameter retrieval without post-processing. Since the system condition number (CN) captures the uniformity and stability properties encoded in the system, we adopt CN as the primary metric for experimental evaluation. The CN value quantifies the perturbations sensitivity of the system, linking detection precision $||\Delta \boldsymbol{S}||/||\boldsymbol{S}||$ to $\mathrm{CN}(\mathbf{R})$/SNR (refs. 48–51), where SNR is the signal-to-noise ratio. In indirect schemes—such as unipolar absorption detectors—mathematical constraints impose a CN floor of $\sqrt{3}$ even with increased measurements[52–58]. Additionally, material limitations further restrict achievable discrimination and extinction ratios (Supplementary Note 5).

We reported a responsivity zeroing strategy by engineering spatial near-field profiles in bar-shaped plasmonic elements. Simulations predict a CN of approximately 1.10 (Supplementary Note 6), and experimental measurements yield a CN of 1.69 (Supplementary Fig. 8). Both results surpass the $\sqrt{3}$ lower bound associated with indirect detection schemes, showing that our approach achieves near-optimal conditioning even under fabrication imperfections. The ability to maintain a low CN experimentally confirms that direct mapping architectures can preserve the essential features of an optimal design despite practical limitations. This supports the feasibility of robust full-Stokes detection at the device level, ensuring stable operation in the presence of noise and variability.

Although we do not eliminate all system complexity, we aimed to reshape the complexity distribution of the system. In reconfigurable single-pixel systems, the structure is relatively simple, and

complexity is allocated primarily to data-driven or learning-based reconstruction[20,21,27,59], whereas multipixel architectures, despite leveraging structured optical encoding, still require numerical inversion or post-processing[23,25,26,33]. By contrast, our method structurally embeds complexity into optical encoding, establishing a one-to-one mapping of each Stokes parameter to a dedicated channel, thereby eliminating computational decoding and enabling real-time operation. Moreover, the four sub-detectors are spaced at subwavelength distances within a single device footprint, enabling near-simultaneous and spatially co-registered measurement of all four Stokes parameters.

Our detector also operates under zero bias, resulting in zero quiescent power consumption at the pixel level. No back-end computation is required, which simplifies integration and supports deployment in power-constrained scenarios. Combined with room-temperature compatibility and a compact, integrated layout, the system is well suited for embedded, power-constrained and field-deployable polarimetric mid-infrared sensing platforms.

Methods

Simulation

The near-field profiles of our nanostructures were simulated with the finite-difference time-domain method (FDTD Solutions package, Lumerical). The periodic boundary condition is set at x and y boundaries and perfect match layer condition is set at the z boundaries. The near-field-driven currents in graphene were simulated using the Python code by solving the Navier–Stokes equations. The MATLAB code used for optimizing the CN under absorption constraints are modulated based on RPSA[60].

Fabrication

Few-layer graphene from natural graphite crystal (NGS Naturgraphit) was mechanically exfoliated onto a thermally oxidized (~285 nm) Si wafer (10 kΩ cm, Nova Electronic Materials). Metallic alignments were fabricated onto the wafer by electron-beam lithography (JBX-6300FS, Jeol; electron-beam resist: *poly(methyl methacrylate)* (PMMA, 495K A5) at 4,000 rpm, 180 °C, 2 min; exposure dose/l 1,300 μC cm^{-2}; develop in *methyl isobutyl ketone* (MIBK):*isopropyl alcohol* (IPA) = 1:3 for 30 s and rinse in IPA for 30 s) and thermal deposition of 5-/20-nm Cr/Au (Kurt J. Lesker Company) and lift-off in hot acetone at 65 °C for 1 h. The graphene is then patterned into regular shapes by electron-beam lithography and oxygen-plasma etching (20-s.c.c.m. O_2, 20 W, 20 s, Vita-Mini RIE system Femto Science), followed by an annealing process at 300 °C for 6 h in an Ar/H_2 atmosphere to remove the resistant residues. Then, metallic nanostructures, contact electrodes and large electrodes were fabricated onto graphene flakes by a third electron-beam lithography process and a second thermal deposition (5-/60-nm Pd/Au) and lift-off process. For the metasurface-based phase plate, the CaF_2 wafer was first cleaned by sonicating in acetone for 10 min, followed by rinsing in IPA and drying under nitrogen. Subsequently, the wafer was coated with an electron-beam lithography resist (495K PMMA A5). To address the insulating nature of the CaF_2 substrate, a thin layer of conducting polymer film ESpacer (Showa Denko) was spin coated at 4,000 rpm. The wafer was then exposed to electron-beam lithography (Jeol 6300FS). Later, the samples were initially immersed in deionized water to remove the ESpacer film and subsequently developed in a MIBK:IPA (1:3) solution for 30 s, followed by a 30-s rinse in IPA. Finally, electron-beam evaporation was used to deposit 5 nm of Ti and 60 nm of Au onto the sample, and a lift-off process in acetone was conducted for 24 h at room temperature

Characterization

A quantum cascade laser at a wavelength of 4 μm (MIRCat-1200, Daylight Solutions; polarization ratio, >100:1) was used as our light source with modulation by an optical chopper (Stanford Research Systems, SR540) at 273 Hz. A low-order half-wave plate (WPLH05M-4000, Thorlabs) and quarter-wave plate (WPLQ05M-4000, Thorlabs) designed at 4 μm were used to control the polarization states of light. An off-axis parabolic mirror (focal length, 101.6 mm; MPD149-P01, Thorlabs) was used to focus and direct light onto our device with normal incidence. The open-circuit voltages were measured as the photoresponse with a lock-in amplifier (filter slope of 24 dB octave^{-1}; Stanford Research Systems, SR830). A time constant of 30 ms is used for noise measurements. The d.c. current–voltage curves were measured using a Keithley 4200-SCS parameter analyser. An oscilloscope (InfiniiVision DSOX3034A, Keysight, 350 MHz, 4 GSa s^{-1}) was used to characterize the on–off cycles and response time of the device. The 1,000-ns pulse was generated by the quantum cascade laser in the pulse mode. The incident power was calibrated using a power meter (843-R, Newport).

Data availability

Source data are provided with this paper. Other data that support the findings of this study are available from the corresponding authors upon reasonable request.

References

1. Jiang, J., Chen, M. & Fan, J. A. Deep neural networks for the evaluation and design of photonic devices. *Nat. Rev. Mater.* **6**, 679–700 (2021).
2. Gopakumar, M. et al. Full-colour 3D holographic augmented-reality displays with metasurface waveguides. *Nature* **629**, 791–797 (2024).
3. Pestourie, R. et al. Physics-enhanced deep surrogates for partial differential equations. *Nat. Mach. Intell.* **5**, 1458–1465 (2023).
4. Rudy, S. H., Brunton, S. L., Proctor, J. L. & Kutz, J. N. Data-driven discovery of partial differential equations. *Sci. Adv.* **3**, e1602614 (2017).
5. Bar-Sinai, Y., Hoyer, S., Hickey, J. & Brenner, M. P. Learning data-driven discretizations for partial differential equations. *Proc. Natl Acad. Sci. USA* **116**, 15344–15349 (2019).
6. Ma, W. et al. Deep learning for the design of photonic structures. *Nat. Photon.* **15**, 77–90 (2021).
7. Ballard, Z., Brown, C., Madni, A. M. & Ozcan, A. Machine learning and computation-enabled intelligent sensor design. *Nat. Mach. Intell.* **3**, 556–565 (2021).
8. Melati, D. et al. Mapping the global design space of nanophotonic components using machine learning pattern recognition. *Nat. Commun.* **10**, 4775 (2019).
9. Shi, L. et al. Towards real-time photorealistic 3D holography with deep neural networks. *Nature* **591**, 234–239 (2021).
10. Deng, J. et al. An on-chip full-Stokes polarimeter based on optoelectronic polarization eigenvectors. *Nat. Electron.* **7**, 1004–1014 (2024).
11. Fröch, J. E. et al. Real time full-color imaging in a meta-optical fiber endoscope. *eLight* **3**, 13 (2023).
12. Liu, C. et al. A programmable diffractive deep neural network based on a digital-coding metasurface array. *Nat. Electron.* **5**, 113–122 (2022).
13. Feng, X. et al. Differential perovskite hemispherical photodetector for intelligent imaging and location tracking. *Nat. Commun.* **15**, 577 (2024).
14. Bansal, S. et al. Optoelectronic performance prediction of HgCdTe homojunction photodetector in long wave infrared spectral region using traditional simulations and machine learning models. *Sci. Rep.* **14**, 28230 (2024).
15. Fang, X. et al. Orbital angular momentum-mediated machine learning for high-accuracy mode-feature encoding. *Light Sci. Appl.* **13**, 49 (2024).
16. Shastri, B. J. et al. Photonics for artificial intelligence and neuromorphic computing. *Nat. Photon.* **15**, 102–114 (2021).

17. Colburn, S., Zhan, A. & Majumdar, A. Metasurface optics for full-color computational imaging. *Sci. Adv.* **4**, eaar2114 (2018).
18. Dong, Y. et al. Achromatic single metalens imaging via deep neural network. *ACS Photonics* **11**, 1645–1656 (2024).
19. Tseng, E. et al. Neural nano-optics for high-quality thin lens imaging. *Nat. Commun.* **12**, 6493 (2021).
20. Fang, C., Li, J., Zhou, B. & Li, D. Self-powered filterless on-chip full-Stokes polarimeter. *Nano Lett.* **21**, 6156–6162 (2021).
21. Ma, J. et al. Full-Stokes polarimeter based on chiral perovskites with chirality and large optical anisotropy. *Small* **17**, 2103855 (2021).
22. Gao, Y. et al. High performance polarization-resolved photodetectors based on intrinsically stretchable organic semiconductors. *Adv. Sci.* **10**, 2204727 (2023).
23. Rubin, N. A. et al. Matrix Fourier optics enables a compact full-Stokes polarization camera. *Science* **365**, eaax1839 (2019).
24. Basiri, A. et al. Nature-inspired chiral metasurfaces for circular polarization detection and full-Stokes polarimetric measurements. *Light Sci. Appl.* **8**, 78 (2019).
25. Dai, M. et al. On-chip mid-infrared photothermoelectric detectors for full-Stokes detection. *Nat. Commun.* **13**, 4560 (2022).
26. Arbabi, E., Kamali, S. M., Arbabi, A. & Faraon, A. Full-Stokes imaging polarimetry using dielectric metasurfaces. *ACS Photonics* **5**, 3132–3140 (2018).
27. Ma, C. et al. Intelligent infrared sensing enabled by tunable moiré quantum geometry. *Nature* **604**, 266–272 (2022).
28. Weng, X., Feng, J., Perry, A. & Vuong, L. T. Non-line-of-sight full-Stokes polarimetric imaging with solution-processed metagratings and shallow neural networks. *ACS Photonics* **10**, 2570–2579 (2023).
29. Fan, Y. et al. Dispersion-assisted high-dimensional photodetector. *Nature* **630**, 77–83 (2024).
30. Foreman, M. R., Favaro, A. & Aiello, A. Optimal frames for polarization state reconstruction. *Phys. Rev. Lett.* **115**, 263901 (2015).
31. Fedorov, V. V. *Theory of Optimal Experiments* (Elsevier, 2013).
32. Li, X., Hu, H., Goudail, F. & Liu, T. Fundamental precision limits of full Stokes polarimeters based on DoFP polarization cameras for an arbitrary number of acquisitions. *Opt. Express* **27**, 31261–31272 (2019).
33. Li, L. et al. Monolithic full-Stokes near-infrared polarimetry with chiral plasmonic metasurface integrated graphene–silicon photodetector. *ACS Nano* **14**, 16634–16642 (2020).
34. Fan, Q. et al. Disordered metasurface enabled single-shot full-Stokes polarization imaging leveraging weak dichroism. *Nat. Commun.* **14**, 7180 (2023).
35. Pukelsheim, F. *Optimal Design of Experiments* (SIAM, 2006).
36. Zhang, B. Y. et al. Broadband high photoresponse from pure monolayer graphene photodetector. *Nat. Commun.* **4**, 1811 (2013).
37. Koepfli, S. M. et al. Metamaterial graphene photodetector with bandwidth exceeding 500 gigahertz. *Science* **380**, 1169–1174 (2023).
38. Pettine, J., et al. Light-driven nanoscale vectorial currents. *Nature* **626**, 984–989 (2024).
39. Giovannetti, G. et al. Doping graphene with metal contacts. *Phys. Rev. Lett.* **101**, 026803 (2008).
40. Zuev, Y. M., Chang, W. & Kim, P. Thermoelectric and magnetothermoelectric transport measurements of graphene. *Phys. Rev. Lett.* **102**, 096807 (2009).
41. Gabor, N. M. et al. Hot carrier–assisted intrinsic photoresponse in graphene. *Science* **334**, 648–652 (2011).
42. Wei, J. et al. Zero-bias mid-infrared graphene photodetectors with bulk photoresponse and calibration-free polarization detection. *Nat. Commun.* **11**, 6404 (2020).
43. Barba, L. A. & Forsyth, G. F. CFD Python: the 12 steps to Navier-Stokes equations. *J. Open Source Educ.* **2**, 21 (2018).
44. Wei, J. et al. Geometric filterless photodetectors for mid-infrared spin light. *Nat. Photon.* **17**, 171–178 (2023).
45. Wei, J. et al. Mid-infrared semimetal polarization detectors with configurable polarity transition. *Nat. Photon.* **15**, 614–621 (2021).
46. Yu, N. et al. Light propagation with phase discontinuities: generalized laws of reflection and refraction. *Science* **334**, 333–337 (2011).
47. Hao, J. et al. Direct detection of circularly polarized light using chiral copper chloride–carbon nanotube heterostructures. *ACS Nano* **15**, 7608–7617 (2021).
48. Yu, Z., Veronis, G., Fan, S. & Brongersma, M. L. Design of midinfrared photodetectors enhanced by surface plasmons on grating structures. *Appl. Phys. Lett.* **89**, 151116 (2006).
49. Bhat, R. D. R., Panoiu, N. C., Brueck, S. R. J. & Osgood, R. M. Enhancing the signal-to-noise ratio of an infrared photodetector with a circular metal grating. *Opt. Express* **16**, 4588–4596 (2008).
50. Li, S. et al. Ultrasensitive, superhigh signal-to-noise ratio, self-powered solar-blind photodetector based on n-Ga_2O_3/p-CuSCN core–shell microwire heterojunction. *ACS Appl. Mater. Interfaces* **11**, 35105–35114 (2019).
51. Householder, A. S. Unitary triangularization of a nonsymmetric matrix. *J. ACM* **5**, 339–342 (1958).
52. Hu, Q., Qiu, Z., Cui, W. & Hong, J. Optimum angles for a full-Stokes scanning polarimeter. *Appl. Opt.* **58**, 4277–4282 (2019).
53. Ambirajan, A. & Look, D. C. Jr. Optimum angles for a polarimeter: part I. *Opt. Eng.* **34**, 1651–1655 (1995).
54. Peinado, A. et al. Optimization and performance criteria of a Stokes polarimeter based on two variable retarders. *Opt. Express* **18**, 9815–9830 (2010).
55. Ambirajan, A. & Look, D. C. Jr. Optimum angles for a polarimeter: part II. *Opt. Eng.* **34**, 1656–1658 (1995).
56. Tyo, J. S. Design of optimal polarimeters: maximization of signal-to-noise ratio and minimization of systematic error. *Appl. Opt.* **41**, 619–630 (2002).
57. Tyo, J. S. Noise equalization in Stokes parameter images obtained by use of variable-retardance polarimeters. *Opt. Lett.* **25**, 1198–1200 (2000).
58. Sabatke, D. S. et al. Optimization of retardance for a complete Stokes polarimeter. *Opt. Lett.* **25**, 802–804 (2000).
59. Liu, T. et al. Deep learning-based holographic polarization microscopy. *ACS Photonics* **7**, 3023–3034 (2020).
60. Liu, X., Kong, X. & Qiu, C.-W. Relative-phase simulated annealing for time-efficient and large-scale inverse design of achromatic thin lenses. *Opt. Express* **30**, 30536–30551 (2022).

Acknowledgements

This work was supported by the National Research Foundation of Singapore (NRF-CRP26-2021-0004, NRF-CRP22-2019-0006 and NRF-CRP30-2023-0003, C.-W.Q.) and by the National Natural Science Foundation of China (grant numbers 62450123 and 62375042, J.W.).

Author contributions

X.L., J.W. and C.-W.Q. conceived the project. X.L. and X.K. carried out the theoretical analysis and numerical simulation. X.L. fabricated the samples. X.L., Y.C. and W.L. performed the device characterization. J.L., Z.N., Q.J.W. and C.L. provided scientific input and feedback on data interpretation and paper preparation. C.-W.Q. and J.W. supervised the project and provided overall guidance throughout. All authors discussed the results and commented on the paper.

Competing interests

The authors declare no competing interests.

Additional information

Supplementary information The online version contains supplementary material available at https://doi.org/10.1038/s41928-025-01481-4.

Correspondence and requests for materials should be addressed to Jingxuan Wei or Cheng-Wei Qiu.

Peer review information *Nature Electronics* thanks Hanxiao Cui and the other, anonymous, reviewer(s) for their contribution to the peer review of this work.